Effects of minor Si addition on structural heterogeneity and glass formation of GdDyErCoAl high-entropy bulk metallic glass

Liliang Shao, Qianqian Wang, Lin Xue, Mingyun Zhu, Anding Wang, Junhua Luan, Kuibo Yin, Qiang Luo, Qiaoshi Zeng, Litao Sun, Baolong Shen

PII: S2238-7854(21)00035-1

DOI: https://doi.org/10.1016/j.jmrt.2021.01.035

Reference: JMRTEC 2650

To appear in: *Journal of Materials Research and Technology*

Received Date: 28 October 2020

Revised Date: 5 January 2021

Accepted Date: 9 January 2021

Please cite this article as: Shao L, Wang Q, Xue L, Zhu M, Wang A, Luan J, Yin K, Luo Q, Zeng Q, Sun L, Shen B, Effects of minor Si addition on structural heterogeneity and glass formation of GdDyErCoAl high-entropy bulk metallic glass, *Journal of Materials Research and Technology*, https://doi.org/10.1016/j.jmrt.2021.01.035.

Effects of minor Si addition on structural heterogeneity and glass formation of GdDyErCoAl high-entropy bulk metallic glass

Liliang Shao[a], Qianqian Wang[a], Lin Xue[a], Mingyun Zhu[b], Anding Wang[c], Junhua Luan[c], Kuibo Yin[b], Qiang Luo[a], Qiaoshi Zeng[a], Litao Sun[b], Baolong Shen[a, d,*]

[a] *School of Materials Science and Engineering, Jiangsu Key Laboratory of Advanced Metallic Materials, Southeast University, Nanjing 211189, China*

[b] *SEU-FEI Nano-Pico Center, Key Laboratory of MEMS of Ministry of Education, School of Electronic Science and Engineering, Southeast University, Nanjing 210018, China*

[c] *Center for Advanced Structural Materials, Department of Mechanical and Biomedical Engineering, College of Science and Engineering, City University of Hong Kong, Kowloon, Hong Kong, China*

[d] *Institute of Massive Amorphous Metal Science, China University of Mining and Technology, Xuzhou 221116, China*

*Corresponding author: Baolong Shen

E-mail: blshen@seu.edu.cn

Abstract

Glass-forming ability (GFA) of the $Gd_{20}Dy_{20}Er_{20}Co_{20}Al_{20}$ high-entropy bulk metallic glass (HE-BMG) was improved through microalloying Si element. The critical diameter of this rare-earth-based HE-BMG increases from 1.5 to 8.5 mm with 0.5 at.% Si addition without any deterioration of magnetocaloric property. Compared with the Si-free sample, the BMG with 0.5 at.% Si addition exhibits low driving force for crystallization, strong supercooled liquid behavior and sluggish crystallization kinetics, whereas excessive Si addition leads to reverse variations. Furthermore, microalloying Si can enhance nanoscale heterogeneity of elemental distribution, and thus facilitates the formation of local crystal-like structures. The connectivity and competition between icosahedra-like clusters and crystal-like structures promote the formation of stable network structure which frustrates crystallization. As Si content is excessive, icosahedra-like cluster is consumed by the further grown crystal-like structure, leading to the destruction of network and decreasing GFA. This work not only elucidates the underlying mechanism of the GFA enhanced by microalloying, but also sheds light on improving the GFA of HE-BMGs through altering nanoscale elemental distribution and structural heterogeneity.

Keywords: Rare-earth-based high-entropy bulk metallic glass; Glass-forming ability; Microalloying; Thermophysical characterization; Structural heterogeneity.

1. Introduction

High-entropy alloys (HEAs) have attracted extensive attentions due to their unique compositions, microstructures and adjustable properties [1-4]. Generally, HEAs stabilize as the simple solid solution phase of body-centered cubic or face-centered cubic rather than intermediate phases. Sometimes, HEA system could also lead to the formation of bulk metallic glass under rapid enough cooling rate, which is defined as high-entropy bulk metallic glass (HE-BMG) [3,4]. According to confusion principle [5], HE-BMGs are supposed to possess improved glass-forming ability (GFA) and it is true that the diameters of some high-entropy bulk metallic glasses (HE-BMGs) are centimeter level [6,7]. However, based on Adam-Gibbs theory, high configurational entropy in HE-BMGs would lead to low viscosity of equilibrium melts [8], and therefore decreases the GFA. Recent studies evidence that the high mixing entropy tend to deteriorate the GFA of HE-BMGs [9,10]. This controversy makes the improvement of GFA for HE-BMGs a knotty problem. HE-BMGs exhibit some unique properties such as high strength, large elastic limits, good corrosion and wear resistance as well as good magnetic properties [3,11,12]. As a typical representative of HE-BMGs, rare-earth (RE)-based HE-BMGs are promising candidates for magnetic refrigerants due to their good magnetocaloric effect. Compared with conventional gas refrigerants, they have advantages of both high efficiency and environmental friendliness [13-15]. However, the GFA of RE-based HE-BMGs is not high enough, limiting their potential applications. Accordingly, it is of great significance to improve the GFA of RE-based HE-BMGs without deteriorating their good magnetocaloric properties.

It is known that component sensitivity is a prominent feature of GFA for BMGs [16,17]. GFA can be enhanced obviously through minor adjustment of composition such as microalloying (usually less than 2 at.%) some elements which can introduce large negative enthalpy of mixing [18]. For example, the critical diameter (d_c) of CuZr- and Fe-based BMGs were enhanced by more than 2 times with minor addition of Y element [19,20]. Besides, doping 0.5 at.% Co or 1 at.% Nb elements improved the GFA of CeCuAl BMG to centimeter level [21,22]. However, several questions for the microalloying effect on GFA need further investigations. Firstly, few studies regarding the effect of microalloying on the GFA of HE-BMGs have been reported, and it remains unclear whether microalloying is also effective to improve the GFA of HE-BMGs. Secondly, the structural evolution induced by microalloying is still elusive. Although the number of crystal-like structures was reported to increase with microalloying [23], the interplay between crystal-like structure and other special clusters such as icosahedra-like cluster needs more detailed investigations. Besides, the elemental distribution is of importance to the heterogeneity in MGs [24-26], but its role in the effect of microalloying on GFA has not been studied in depth. Thirdly, the underlying mechanism of the positive impact with minor addition, but negative influence through excessive addition on GFA is still unclear [27]. Therefore, it may be an effective method to improve the GFA of HE-BMGs through microalloying and more in-depth investigations are necessary to unveil the effect of microalloying on GFA.

In our previous work, a quinary $Gd_{20}Dy_{20}Er_{20}Co_{20}Al_{20}$ HE-BMG with good magnetocaloric property was fabricated, but its d_c was only 1.5 mm [14]. Si element has large negative enthalpy of mixing with some heavy RE elements, such as Gd, Dy and Er [28]. Besides, it has been reported that the structural topology of amorphous silicon fits with the continuous random network model, which is more difficult to be broken down during glass transition [29,30]. Therefore, minor Si element was added to $Gd_{20}Dy_{20}Er_{20}Co_{20}Al_{20}$ HE-BMG with the aim of improving its GFA in this study. As a result, the d_c of this RE-based HE-BMG was successfully improved from 1.5 to 8.5 mm with 0.5 at.% Si addition without deteriorating its good magnetocaloric property. However, excessive Si addition led to the fateful decrease of GFA. Thermophysical properties based on thermodynamics and kinetics such as linear thermal expansion, specific capacity and kinetic fragility were carefully characterized to investigate the variation of GFA with Si addition. The underlying structural origin of the change of GFA caused by Si addition was studied from the perspective of nanoscale heterogeneity including elemental distribution and local favored structures.

2. Experimental methods

The $(Gd_{0.2}Dy_{0.2}Er_{0.2}Co_{0.2}Al_{0.2})_{100-x}Si_x$ (x = 0, 0.5, 1, 2, 3 and 4) master alloy ingots were prepared by arc-melting a mixture of pure metals in a high-purity argon atmosphere. The purity of Gd, Dy and Er metals used in this study is above 99.9%, and that of Co, Al and Si elements is above 99.99%. Each ingot was re-melted for five times to ensure chemical homogeneity. Eventually, copper mold casting was used to fabricate BMG samples with different diameters.

The amorphous nature of the as-cast sample was ascertained by X-ray diffraction (XRD, Bruker D8 Discover) using Cu Kα radiation. The microstructures of BMG samples were investigated by a spherical aberration-corrected transmission electron microscope (TEM, Titan 80-300). The specimens for TEM observation were prepared by mechanical polishing and Ar ion milling (PIPS 691, Gatan) at 3.0 keV cooled by liquid nitrogen. The elemental distributions on macro scale and nanoscale were analyzed by energy-dispersive X-ray spectroscopy (EDS) in scanning electron microscopy (SEM, FEI Sirion 200) and TEM, respectively. Reduced density function (RDF) was calculated by analyzing diffraction patterns using the Gatan Digital Micrograph software with the PASAD-tools [31,32]. Besides, the nanoscale elemental distribution was also investigated by three-dimensional atom probe tomography (3D-APT) in a local electrode atom probe (CAMEACA LEAP 5000 XR). Needle-shaped specimens required for APT were fabricated by lift-outs and annular milled in a FEI Scios focused ion beam/scanning electron microscope (FIB/SEM). Imago Visualization and Analysis Software (IVAS) version 3.8 was used for the 3D reconstructions and data analysis.

The temperature and field dependences of the magnetization were measured using a SQUID magnetometer (MPMS, Quantum Design). Samples with a diameter of 1 mm were used for magnetic measurements. In an isothermal magnetization (M-H) process, the total magnetic entropy change (ΔS_M) of samples can be calculated by integrating the Maxwell relation [33].

Thermal analyses were performed on a differential scanning calorimeter (DSC, Netzsch DSC 404 F3). The characteristic temperatures such as the onsets of glass transition (T_g), of crystallization (T_x), of melting (T_m) and the end of glass transition (T_g^{end}) were determined using the tangent construction method. Enthalpies of crystallization and fusion were calculated by integrating the corresponding DSC peaks. Isothermal crystallization was performed on a DSC (PerkinElmer DSC 8500). Amorphous samples were heated to the target temperature (T_g^{end}+5 K) with a heating rate of 500 K/min, and then kept isothermal until the end of crystallization.

Specific heat capacities (C_p) for glassy, crystalline and liquid states were measured using a temperature step method [34-36]. Firstly, the samples were polished into disk with the mass of 25 mg to realize good thermal conductivity. Then, samples were heated with a series of temperature steps of 10 K under a heating rate of 20 K/min alternating with isothermal sections of 10 min. The C_p values were obtained by comparing the resulting steps in the heat flow of the samples with those of a sapphire standard and an empty pan. The temperature dependence of C_p curves for liquid ($C_p^l(T)$) and crystal ($C_p^x(T)$) were fitted using the following equations, respectively [37]:

$$C_p^l(T) = 3R + aT + bT^{-2} \tag{1}$$

$$C_p^x(T) = A + 3R + cT + dT^2 \tag{2}$$

where R is the universal gas constant, a, b, c, d and A are fitting constants. Then, the functions of enthalpy difference ($\Delta H^{l-x}(T)$), entropy difference ($\Delta S^{l-x}(T)$) and the Gibbs free energy difference between liquid and crystal (ΔG^{l-x}) were calculated.

The linear thermal expansion curves were obtained by a thermomechanical analyzer (TMA, Netzsch TMA 402 F3) through dilatometric measurements. BMG samples with a diameter of 1.5 mm and a height of 3 mm were heated from room temperature to 903 K with a heating rate of 20 K/min under a constant applied force of 0.2 N. The kinetic viscosity (η) was then calculated according to $\eta = \sigma/(3\dot{\varepsilon})$ with σ and $\dot{\varepsilon}$ the stress and strain rate respectively [38].

3. Results and discussion

3.1 Glass-forming ability and magnetocaloric effect

Figure 1(a) shows the DSC curves of $(Gd_{0.2}Dy_{0.2}Er_{0.2}Co_{0.2}Al_{0.2})_{100-x}Si_x$ HE-BMG samples with a diameter of 1 mm. The supercooled liquid region (SCLR) is broadened by 22 K with only 0.5 at.% Si addition, and this value is 28 K for $(Gd_{0.2}Dy_{0.2}Er_{0.2}Co_{0.2}Al_{0.2})_{99}Si_1$ HE-BMG as listed in Table 1. With the further increase of Si content, T_g moves to higher temperature, but the values of T_x keep almost unchanged, leading to the decrease of SCLR. The melting behaviors of HE-BMGs were also studied by DSC as shown in Fig. 1(b). It can be seen that the DSC curves for samples with minor Si addition show a single peak upon heating whereas for samples with Si content higher than 2 at.% exhibit multiple endothermic melting peaks, indicating that the HEAs with excessive Si addition are far away from their eutectic compositions. Moreover, the parameters including reduced glass transition temperature T_{rg} (= T_g/T_l) and gamma parameter γ (= $T_x/(T_g+T_l)$) are calculated as listed in Table 1. Larger values of T_{rg} and γ correspond to the higher stability of liquids, which is beneficial to the glass formation [39,40]. In this study, microalloying 0.5 and 1 at.% Si enhance the T_{rg} and γ simultaneously, indicating that these alloys possess higher stability to inhibit crystallization during cooling. On the contrary, both T_{rg} and γ decrease gradually as the Si content increase from 1 to 4 at.%. This means that the HEAs with excessive Si addition possess lower thermal stability upon cooling. Therefore, it is expected that the GFA of the studied HE-BMG is improved with minor Si addition and the $(Gd_{0.2}Dy_{0.2}Er_{0.2}Co_{0.2}Al_{0.2})_{100-x}Si_x$ (x = 0.5 or 1) HE-BMG possesses the largest d_c. Subsequently, copper mold casting was performed to evaluate the GFA of these HE-BMGs. Hereafter, $(Gd_{0.2}Dy_{0.2}Er_{0.2}Co_{0.2}Al_{0.2})_{100-x}Si_x$ are denoted as HESix.

Consistent with the prediction of DSC curves, the best glass former is obtained with 0.5 at.% Si addition. The corresponding XRD patterns for HESi0.5 and HESi1 BMG samples are shown in Fig. 1(c). Two broad humps without sharp crystalline peak for the as-cast HESi0.5 samples with diameters of 5 and 8.5 mm identify their amorphous structures. Moreover, only unobvious crystalline peaks are observed in the XRD pattern of the HESi0.5 sample with diameter of 10 mm as shown in Fig. 1(d), and thus the d_c of HESi0.5 BMG is ascertained as 8.5 mm. Similarly, the d_c of HESi1 BMG is identified as 6 mm. With excessive Si addition, GFA drops gradually and the d_c is only 1 mm with 4 at.% Si addition. Besides, one can see from Fig. 1(d) that the crystallization products of the HEAs with different Si content are distinct. Due to the multiple components, considerable crystalline phases precipitate in the as-cast HESi0 sample with a diameter of 2 mm. The main crystallization products are composed of Al-Co, Al-RE and Co-RE phases. Different form the HESi0, only several inconspicuous crystalline peaks can be detected for the as-cast HESi0.5 sample with the diameter of 10 mm. Besides, some Si-containing phases such as $GdCoSi_2$ and Co_2AlSi_2 precipitate simultaneously. These phases compete with the Si-free phases such as Al_2Gd_3 and Al_3Dy upon cooling from metallic melt, which can inhibit the crystallization process, and thus lead to a better GFA. However, crystallization becomes obvious again for the as-cast HESi3 sample with the diameter of 4 mm. Since the large negative enthalpy of mixing between Si and other components, multiple Si-containing phases tend to precipitate preferentially with excessive Si addition. That is to say, the competition between Si-free and Si-containing phases is not enough to stable the glass-forming liquid, i.e. leading to the deterioration of GFA.

Heavy RE-based BMGs have been considered as potential magnetocaloric materials because of their good magnetocaloric effect [36,41]. Compared with the HESi0 sample, no evident distinctions on the Curie temperature (T_C), the maximum value of magnetic entropy change ($|\Delta S_M^{pk}|$) and the relative cooling power (*RCP*) [42] for samples with minor Si addition can be seen, as listed in Table 2. Consequently, the GFA of RE-based HE-BMG is enhanced by microalloying Si element without deterioration of its magnetocaloric property in this study.

3.2 Thermodynamic and kinetic analyses

Compared with most microalloying systems [16], the fluctuation of GFA and SCLR induced by Si addition in this HE-BMG is more distinct. Besides, due to the inconformity between the width of SCLR and GFA, more comprehensive thermodynamic characterizations need to be performed to investigate the impact of minor Si addition on GFA. Fig. 2 shows the isothermal crystallization curves in SCLR. It is clear that HESi0.5 sample possesses the longest incubation time (t_{in} in the figure), approximately one order of magnitude larger than that of HESi0 sample, and the most sluggish crystallization process. As the Si content exceeds 0.5 at.%, both the incubation time and total crystallization time decrease but are still longer than those of HESi0, indicating that microalloying Si appropriately can enhance the crystallization resistance of BMGs.

The driving force for crystallization plays an essential role in glass transition, which can be quantified by ΔG^{l-x}. To obtain relative accurate values of ΔG^{l-x}, the C_p data of glassy, liquid (supercooled and stable liquids) and crystalline states were measured and fitted according to Eqs. (1) and (2), as shown in Fig. 3. The corresponding fitting parameters are listed in Table 2. All of the samples show a step of C_p in the glassy term around T_{g}, corresponding to a typical glass transition. With the increase of Si content, the value of C_p for glass raises gradually and exhibits an identical trend with T_{g} as shown in Fig. 1(a), implying Si addition enhances the thermal stability of the HE-BMG. The calculated $\Delta G^{l-x}(T)$ curves of HESix alloys are shown in Fig. 4. It is seen that microalloying Si reduces $\Delta G^{l-x}(T)$, especially for HESi0.5 sample. With excessive Si addition such as HESi1, $\Delta G^{l-x}(T)$ increases as expected. In general, $\Delta G^{l-x}(T)$ could basically scale with GFA in the same alloy system. Nevertheless, there will be some exceptions due to the extreme complexity of glass transition and the effect of high entropy, i.e. HESi3 sample possesses the lowest $\Delta G^{l-x}(T)$ approaching to T_{g}. This indicates that the effect of Si addition on GFA cannot be elucidated comprehensively just from the framework of thermodynamics in this HE-BMG system. Glass transition is the consequence of the interplay between thermodynamics and kinetics of crystal nucleation, more precisely, of the competition between driving force for crystallization and liquid fragility [43]. Accordingly, the effect of kinetics on GFA should also be studied.

The kinetic fragility is regarded as a powerful index to evaluate the properties of supercooled liquid, such as fragility parameter (D^*). According to that, liquids are divided roughly into two categories, i.e., fragile or strong [44]. In order to obtain D^* of the studied glass formers, dilatometric measurements were performed and the corresponding TMA traces are shown in Fig. 5(a). At low temperatures, the configurational contribution to thermal expansion is structurally frozen, and the vibration dominates the thermal expansion process, thus all the studied BMGs show almost the same expansion behavior. While in SCLR, the configurational contribution becomes more prominent with the increase of temperature, leading to a softening behavior [45]. It is clear that Si addition changes the softening behavior, indicating a distinct variation of viscosity in SCLR. The kinetic viscosity is calculated and fitted with Vogel-Fulcher-Tammann (VFT) equation [44]:

$$\eta(T) = \eta_0\, exp\left(\frac{D^{*}T_0}{T - T_0}\right) \tag{3}$$

where D^* is the fragility parameter and T_0 is the VFT-temperature. The data and fitting results are displayed in Fig. 5(b). For the HESix system, the values of D^* are highly consistent with the thermal stability characterized by crystallization kinetics and GFA of HE-BMGs, i.e., larger value of D^* corresponds to better GFA. The HESi0.5 sample exhibits the most sluggish kinetics, indicative of the lowest atomic mobility, which leads to the largest resistance of atomic rearrangement. Under the interplay of thermodynamics and kinetics, crystallization is suppressed by glass transition and the GFA is improved with minor Si addition.

3.3 Heterogeneity of elemental distribution

The thermodynamic and kinetic origin of the improved GFA induced by microalloying is elucidated from in-depth thermophysical analyses, which can provide theoretical guidelines to design new type of HE-BMGs with better GFA. Nevertheless, the underlying mechanism of microalloying effect on GFA from the structural viewpoint needs further investigations. Heterogeneity is essential for the modification of various properties of BMGs [24]. In HE-BMGs, the structural heterogeneity is also reported to play a significant role in tailoring the mechanical properties [11,46], and can be tuned by microalloying [11]. To visualize the potential heterogeneity, elemental distributions of the HE-BMG samples with different Si contents were characterized. However, SEM-EDS mappings reveal homogeneous distribution of all elements for HESi0, HESi0.5 and HESi3 BMG samples as shown in Fig. 6(a)-(c), which indicates that no detectable segregation on macroscopic scale is caused by doping Si. This guarantees the reliability and stability of microalloying Si to improve GFA of BMG. For nanoscale elemental distribution, high-angle annular dark field scanning TEM (HAADF STEM) image and corresponding EDS mappings of HESi0, HESi0.5 and HESi3 BMG samples are shown in Fig. 6(d)-(f). No indication of elemental clustering or phase segregation is observed for the samples. However, compared with HESi0 and HESi3 BMGs, HESi0.5 BMG shows more obvious elemental fluctuation, i.e., some degree of heterogeneity. To quantify this elemental fluctuation or heterogeneity, the corresponding elemental distributions along the diagonal of EDS mappings in Fig. 6(d)-(f) are derived and shown in Fig. 7(a)-(c), respectively. For comparison, the intensity axes are normalized by dividing the largest value of each distribution curve. It is clear that the fluctuation of elemental distribution for HESi0.5 BMG is more distinct than those of HESi0 and HESi3 BMGs. Besides, the elemental concentration of the first 40 nm is slightly higher than that of the latter, indicating an enhanced heterogeneity in the HESi0.5 BMG as well.

3D-APT was also performed to characterize the elemental distribution. The corresponding reconstructions of all elements for HESi0, HESi0.5 and HESi3 BMG samples are shown in Fig. 8(a)-(c), respectively. All elements exhibit a random and homogeneous distribution especially for HESi0 and HESi3 BMGs. For HESi0.5 BMG sample, the distribution of Si element seems to be heterogeneous to some extent, but no evident cluster is observed. One-dimensional concentration profiles of all elements are shown in Fig. 8(e) and (f). Although there is slight fluctuation of elemental fractions along the length direction of the tip, the overall distributions remain homogeneous. And the compositions confirmed by 3D-APT are in agreement with the nominal compositions of the HE-BMGs. Furthermore, the statistical binomial frequency distribution analyses in Fig. 8(g) and (h) show that the binomial fitting curves match well with the experimental data for the samples. The values of the normalized homogenization parameter μ for the elements are less than 1, indicating that no nanoscale atomic cluster is detected [47]. Nevertheless, the values of μ for Si and Co elements are much larger than those of others, implying a certain heterogeneity of the distribution for these two elements. According to the elemental distribution analyses through 3D-APT, although no nanoscale cluster is observed in the detected tips, elemental fluctuation and heterogeneous inclination exist especially for Si-containing samples, which is consistent with the STEM-EDS analyses. This heterogeneity of elemental distribution is conducive to producing some local favored structures [48,49].

3.4 Structural heterogeneity

Fig. 9(a)-(c) shows the typical HRTEM images and selected area electron diffraction (SAED) patterns of HESi0, HESi0.5 and HESi3 BMG samples. The maze-like structure and halo-like pattern identify the overall amorphous state of the samples. However, as marked by white boxes in Fig. 9(b) and (c), some local crystal-like structures characterized by a fringe patterns, which is representative of translational symmetry, are observed in HESi0.5 and HESi3 BMGs. To obtain the statistical analyses of local crystal-like structures, the auto-correlation method is performed [50,51]. The HRTEM images selected by yellow squares in Fig. 9(a)-(c) are divided into 100 sub-images, thus each cell has dimension of 1.811 × 1.811 nm^2, similar to the size of the observed crystal-like order. From the corresponding 2D auto-correlation mappings shown in Fig. 9(d)-(f), we calculate the total areal fraction of the crystal-like structure. This value is 12% for HESi0 BMG and increases to 23% and 26% for HESi0.5 and HESi3 BMGs, respectively, which is consistent with the result reported in CuZr-based BMG [23]. Therefore, the structural heterogeneity of BMGs is enhanced with Si addition due to the increase of crystal-like structure.

It is found that the crystal-like structure is ubiquitous in MGs [23,52,53], and its quantity can be changed via adjusting composition and temperature [52,54], resulting in the modification of structural heterogeneity of MGs [55,56]. From this point of view, the overall improvement of GFA accompanying with low $\Delta G^{l-x}(T)$ and sluggish crystallization with minor Si addition can be well explicated. On the one hand, the increase of local ordering drops the potential energy of system. As shown in Fig. 4, the Si-containing alloys possess lower driving force for crystallization than that of the Si-free sample. On the other hand, the “pining effect” introduced by crystal-like structure impedes the rearrangement of atoms [23], i.e., a higher energy barrier for atomic diffusion is achieved through minor Si addition, leading to a sluggish kinetics. However, it is insufficient to explain the reason for the nonlinear tendency among GFA, thermodynamics, kinetics and doping amount just based on the number of local favored clusters. Further analyses of the clusters need to be carried out.

Fig. 10(a) displays the RDFs obtained from the SAED patterns of HESi0, HESi0.5 and HESi3 BMGs shown in the insets of Fig. 9(a), (b) and (c), respectively. No peak indicating the presence of crystalline phase is detected, which matches well with the HRTEM images. The first maximum peak in the RDFs corresponds to the bond between RE (Gd, Dy, Er) and Al atoms [57]. It is worth noting that the positions of the first maximum peak in this study are slightly larger than the reported results, indicating the existence of some preferential local orders before the first peak. As shown in Fig. 10(b), HESi0 exhibits a shoulder between 2.5 and 3.0 Å corresponding to Co-Al and Al-Al atomic pairs, which is consistent with the result in Ref. [57], and ascribes to the effect of high-entropy [9]. Due to the large enthalpy of mixing between Si and Al elements, the formation Al-Si atomic pair with a bond length of 2.56 Å take precedence over other bonds in the first peak. Therefore, the shoulder becomes more distinguished and moves to lower position with Si addition. Consequently, the local random packing becomes denser and the chemical heterogeneity is increased with Si addition through the formation of preferential Si-containing orders, implying the enhancement of interplay among local structures.

Solute-centered atomic clusters with favorable short-range order have been considered as the basic building blocks for BMGs [58,59]. Based on minimum energy consideration, icosahedral cluster is a favorable configuration when the ratio of solute versus solvent radius (r) is around 0.85 [60]. As the $r_{(\mathrm{Al})}/r_{(\mathrm{Gd,\ Dy,\ Er,\ Co})}$ ratio is estimated to be 0.87 [61,62], the predominant cluster configurations in this HE-BMG could be icosahedra-like Al-centered clusters. Fig. 11 shows the inverse Fourier Transformation (IFT) filtered HRTEM images and the corresponding Fourier Transformation (FT) diffraction patterns of the yellow squares in Fig. 9(a)-(c). All of the samples contain icosahedra-like clusters characterized by spherical symmetry at the length of 1-2 nm such as regions A and B [54,63], and they are well dispersed in the amorphous matrix. Some super-clusters composed of multiple primary icosahedra-like orders are also observed as marked by dashed circles such as region C, which indicates that the connectivity among icosahedra-like clusters is intrinsic for BMGs [64,65]. Because inhomogeneous paracrystalline structures containing local ordering at the length scale of 1-2 nm are inherent in the amorphous silicon [29], Si addition in the HE-BMG promotes the formation of local crystal-like structures as indicated by the white boxes. Besides, the largest size of crystal-like structures raises from 2 to 4 nm with Si content increasing from 0.5 to 3 at.% as shown in Fig. 11(b) and (c). Two bright spots appear on the SAED pattern of HESi3 sample, which is consistent with the pronounced translational symmetry in Fig. 11(c). However, no detectable spot in the SAED is observed for HESi0.5 sample although some crystal-like structures are marked in Fig. 11(b). With the increase of the Si content, these motifs prone to aggregate and connect with each other due to the large negative enthalpy of mixing and size mismatch between Si and other components [66,67], thus the number and scale of crystal-like structures are enhanced.

More importantly, the interplay between icosahedra-like cluster and crystal-like structure is introduced through microalloying Si element, leading to the frustration of atomic rearrangement. On the one hand, the competition between icosahedra-like cluster and crystal-like structure inhibits the growth of translational symmetry [54]. As shown in regions D and E, some fringe patterns meet icosahedra-like clusters at four sides or trap them inside, leading to the frustration of the growth of these crystal-like structures. In this scenario, the icosahedra-like cluster acts mainly as an obstacle to the formation of the global translational symmetry. On the other hand, the crystal-like structure could be in turn regarded as a hinge which enhances the connectivity of icosahedra-like clusters, and promotes the formation of overall network structure. Consequently, the rearrangement of atoms upon glass transition becomes sluggish, that is to say the amorphous structure is stabilized. It is noteworthy that the icosahedra-like clusters remain nearly unaltered and appear mainly on the boundary of crystal-like structures in the HESi0.5 sample. In those places, the pinning effect suppresses the growth of crystal-like order. Even though the icosahedra-like clusters are trapped in long-range orders, the translational symmetry can be broken and transforms to disordered structures attributed to the dominant position of icosahedra-like cluster in the competition with crystal-like structure. However, excessive Si addition reverses this competition, i.e., crystal-like structure becomes dominant. Further extended translational symmetry captures more icosahedra-like clusters and transforms them from spherical symmetry to translational symmetry. The corresponding morphological transformation can be seen in regions F and G, where only parts of the icosahedra-like clusters are preserved. As a result, the crystallization resistance decreases significantly. Due to the existence of some undeveloped crystal-like structures, the interplay between them and icosahedra-like clusters is still not negligible. HESi3 BMG also exhibits a better GFA than HESi0 BMG but worse than HESi0.5 BMG. Thus, the reason why microalloying improves GFA while excessive addition decrease GFA of HE-BMG is well explained from the connectivity and competition between icosahedra-like cluster and crystal-like structure, which is of benefit to explore the structural origin of glass formation and design new type of HE-BMGs with improved GFA.

4. Conclusions

This work provides a practical method to enhance the GFA of HE-BMGs via microalloying, which can break through the controversy of confusion principle and Adam-Gibbs theory while designing HE-BMGs. The critical diameter of $Gd_{20}Dy_{20}Er_{20}Co_{20}Al_{20}$ HE-BMG is improved obviously from 1.5 to 8.5 mm with 0.5 at.% Si addition. From the perspective of thermodynamics, minor Si addition reduces the driving force for crystallization. In terms of kinetics, microalloying leads to strong supercooled liquid behavior and sluggish crystallization kinetics, whereas excessive addition causes opposite changes. Moreover, the nanoscale heterogeneity is correlated with doping amount in this study, which elucidate the structural origin of the positive effect of microalloying and negative effect of excessive addition on GFA. Minor Si addition enhances the nanoscale heterogeneity of elemental distribution. As Si content is excess, the effect of this nanoscale heterogeneity is restrained. Microalloying Si not only increases the fraction of crystal-like structure with the size of 1-2 nm but also promotes the connectivity and competition between icosahedra-like cluster and crystal-like structure, leading to the formation of stable network structure and the frustration of crystallization. However, icosahedra-like cluster is consumed by the further grown crystal-like structure (about 4 nm) with excessive Si addition, and the network structure is broken, resulting in the deterioration of GFA. Hence, it can be concluded that the modification of structural heterogeneity through appropriate microalloying is effective to design new HE-BMGs with improved GFA and good functional properties.

Conflicts of interest

The authors declare no conflicts of interest.

Acknowledgements

We thank Profs. E.S Park and M.Q. Jiang for help in the calculation of RDFs. We also thank J.D. Huang for the measurement of TMA. This work was supported by the National Natural Science Foundation of China (Grant nos. 51631003 and 51871054), and the Fundamental Research Funds for the Central Universities (Grant Nos. 2242019K40183 and 2242019k1G005).

References

[1] Cantor B, Chang ITH, Knight P, Vincent AJB. Microstructural development in equiatomic multicomponent alloys, Mater Sci Eng A 2004;375:213-218. https://doi.org/10.1016/j.msea.2003.10.257.

[2] Yeh JW, Chen SK, Lin SJ, Gan JY, Chin TS, Shun TT, Tsau CH, Chang SY. Nanostructured high-entropy alloys with multiple principal elements: Novel alloy design concepts and outcomes. Adv Eng Mater 2004;6:299-303. https://doi.org/10.1002/adem.200300567.

[3] Zhang Y, Zuo TT, Tang Z, Gao MC, Dahmen KA, Liaw PK, Lu ZP. Microstructures and properties of high-entropy alloys. Prog Mater Sci 2014;61:1-93. https://doi.org/10.1016/j.pmatsci.2013.10.001.

[4] Ye YF, Wang Q, Lu J, Liu CT, Yang Y. High-entropy alloy: challenges and prospects. Mater Today 2016;19:349-362. https://doi.org/10.1016/j.mattod.2015.11.026.

[5] Greer AL. Materials science-confusion by design. Nature 1993;366:303-304. https://doi.org/10.1038/366303a0.

[6] Takeuchi A, Chen N, Wada T, Yokoyama Y, Kato H, Inoue A, Yeh JW. $Pd_{20}Pt_{20}Cu_{20}Ni_{20}P_{20}$ high-entropy alloy as a bulk metallic glass in the centimeter. Intermetallics 2011;19:1546-1554. https://doi.org/10.1016/j.intermet.2011.05.030.

[7] Zhao SF, Shao Y, Liu X, Chen N, Ding HY, Yao KF. Pseudo-quinary $Ti_{20}Zr_{20}Hf_{20}Be_{20}(Cu_{20-x}Ni_x)$ high entropy bulk metallic glasses with large glass forming ability. Mater Des 2015;87:625-631. https://doi.org/10.1016/j.matdes.2015.08.067.

[8] Adam G, Gibbs JH. On temperature dependence of cooperative relaxation propertives in glass-forming liquids. J Chem Phys 1965;43:139-&. https://doi.org/10.1063/1.1696442.

[9] Kim J, Oh HS, Kim J, Ryu CW, Lee GW, Chang HJ, Park ES. Utilization of high entropy alloy characteristics in Er-Gd-Y-Al-Co high entropy bulk metallic glass. Acta Mater 2018;155:350-361. https://doi.org/10.1016/j.actamat.2018.06.024.

[10] Lee JS, Oh HS, Kim W, Ryu CW, Kim JY, Chang HJ, Gu JL, Yao KF, Murty BS, Park ES.

Anomalous behavior of glass-forming ability and mechanical response in a series of equiatomic binary to denary metallic glasses. Materialia 2020;9:100505. https://doi.org/10.1016/j.mtla.2019.100505.

[11] Du Y, Zhou Q, Ren Y, Kuang WW, Han WC, Zhang S, Zhai HM, Wang HF. Tailoring shear banding behaviors in high entropy bulk metallic glass by minor Sn addition: A nanoindentation study. J Alloys Compd 2018;762:422-430. https://doi.org/10.1016/j.jallcom.2018.05.194.

[12] Zhou Q, Du Y, Han WC, Ren Y, Zhai HM, Wang HF. Identifying the origin of strain rate sensitivity in a high entropy bulk metallic glass. Scripta Mater 2019;164:121-125. https://doi.org/10.1016/j.scriptamat.2019.02.002.

[13] Huo JT, Huo LS, Men H, Wang XM, Inoue A, Wang JQ, Chang CT, Li RW. The magnetocaloric effect of Gd-Tb-Dy-Al-M (M = Fe, Co and Ni) high-entropy bulk metallic glasses. Intermetallics 2015;58:31-35. https://doi.org/10.1016/j.intermet.2014.11.004.

[14] Li J, Xue L, Yang WM, Yuan CC, Huo JT, Shen BL. Distinct spin glass behavior and excellent magnetocaloric effect in $Er_{20}Dy_{20}Co_{20}Al_{20}RE_{20}$ (RE = Gd, Tb and Tm) high-entropy bulk metallic glasses. Intermetallics 2018;96:90-93. https://doi.org/10.1016/j.intermet.2018.03.002.

[15] Xue L, Shao LL, Luo Q, Shen BL. $Gd_{25}RE_{25}Co_{25}Al_{25}$ (RE = Tb, Dy and Ho) high-entropy glassy alloys with distinct spin-glass behavior and good magnetocaloric effect. J Alloys Compd 2019;790:633-639. https://doi.org/10.1016/j.jallcom.2019.03.210.

[16] Wang WH. Roles of minor additions in formation and properties of bulk metallic glasses. Prog Mater Sci 2007;52:540-596. https://doi.org/10.1016/j.pmatsci.2006.07.003.

[17] Lucena FA, Kiminami CS, Afonso CRM. New compositions of Fe-Co-Nb-B-Y BMG with wide supercooled liquid range, over 100 K. J Mater Res Technol 2020;9:9174-9181. https://doi.org/10.1016/j.jmrt.2020.06.035.

[18] Lu ZP, Liu CT. Role of minor alloying additions in formation of bulk metallic glasses: A review. J Mater Sci 2004;39:3965-3974. https://doi.org/10.1023/b:Jmsc.0000031478.73621.64.

[19] Xu DH, Duan G, Johnson WL. Unusual glass-forming ability of bulk amorphous alloys based on ordinary metal copper. Phys Rev Lett 2004;92:245504. https://doi.org/10.1103/PhysRevLett.92.245504.

[20] Lu ZP, Liu CT, Thompson JR, Porter WD. Structural Amorphous Steels. Phys Rev Lett 2004;92:049901. https://doi.org/10.1103/PhysRevLett.92.245503.

[21] Zhang B, Wang RJ, Zhao DQ, Pan MX, Wang WH. Superior glass-forming ability through microalloying in cerium-based alloys. Phys Rev B 2006;73:092201. https://doi.org/10.1103/PhysRevB.73.092201.

[22] Zhang B, Zhao DQ, Pan M, Wang RJ, Wang WH. Formation of cerium-based bulk metallic glasses. Acta Mater 2006;54:3025-3032. https://doi.org/10.1016/j.actamat.2006.02.044.

[23] Wang Q, Liu CT, Yang Y, Liu JB, Dong YD, Lu J. The atomic-scale mechanism for the enhanced glass-forming-ability of a Cu-Zr based bulk metallic glass with minor element additions. Sci Rep 2014;4:4648. https://doi.org/10.1038/srep04648.

[24] Guan PF, Wang B, Wu YC, Zhang S, Shang BS, Hu YC, Su R, Liu Q. Heterogeneity: the soul of metallic glasses. Acta Phys Sin 2017;66:176112. https://doi.org/10.7498/aps.66.176112.

[25] Qiao JC, Wang Q, Pelletier JM, Kato H, Casalini R, Crespo D, Pineda E, Yao Y, Yang Y. Structural heterogeneities and mechanical behavior of amorphous alloys. Prog Mater Sci 2019;104:250-329. https://doi.org/10.1016/j.pmatsci.2019.04.005.

[26] Wang WH. Dynamic relaxations and relaxation-property relationships in metallic glasses. Prog

Mater Sci 2019;106:100561.https://doi.org/10.1016/j.pmatsci.2019.03.006.

[27] Xi XK, Li LL, Zhang B, Wang WH, Wu Y. Correlation of atomic cluster symmetry and glass-forming ability of metallic glass. Phys Rev Lett 2007;99:095501. https://doi.org/10.1103/PhysRevLett.99.095501.

[28] Takeuchi A, Inoue A. Classification of bulk metallic glasses by atomic size difference, heat of mixing and period of constituent elements and its application to characterization of the main alloying element. Mater Trans 2005;46:2817-2829. https://doi.org/10.2320/matertrans.46.2817

[29] Treacy MMJ, Borisenko KB. The Local Structure of Amorphous Silicon. Science 2012;335:950-953. https://doi.org/10.1126/science.1214780.

[30] Fan Z, Ding J, Li QJ, Ma E. Correlating the properties of amorphous silicon with its flexibility volume. Phys Rev B 2017;95:144211. https://doi.org/10.1103/PhysRevB.95.144211.

[31] Gammer C, Mangler C, Rentenberger C, Karnthaler HP. Quantitative local profile analysis of nanomaterials by electron diffraction. Scripta Mater 2010;63:312-315. https://doi.org/10.1016/j.scriptamat.2010.04.019.

[32] Ding G, Li C, Zaccone A, Wang WH, Lei HC, Jiang F, Ling Z, Jiang MQ. Ultrafast extreme rejuvenation of metallic glasses by shock compression. Sci Adv 2019;5:eaaw6249. https://doi.org/10.1126/sciadv.aaw6249.

[33] Hashimoto T, Numasawa T, Shino M, Okada T. Magnetic refrigeration in the temperature-range from 10 K to room-temperature-the ferromagnetic refrigerants. Cryogenics 1981;21:647-653. https://doi.org/10.1016/0011-2275(81)90254-x.

[34] Busch R, Liu W, Johnson WL. Thermodynamics and kinetics of the $Mg_{65}Cu_{25}Y_{10}$ bulk metallic glass forming liquid. J Appl Phys 1998;83:4134-4141. https://doi.org/10.1063/1.367167.

[35] Gallino I, Shah MB, Busch R. Enthalpy relaxation and its relation to the thermodynamics and crystallization of the $Zr_{58.5}Cu_{15.6}Ni_{12.8}Al_{10.3}Nb_{2.8}$ bulk metallic glass-forming alloy. Acta Mater 2007;55:1367-1376. https://doi.org/10.1016/j.actamat.2006.09.040.

[36] Shao LL, Xue L, Luo Q, Wang QQ, Shen BL. The role of Co/Al ratio in glass-forming GdCoAl magnetocaloric metallic glasses. Materialia 2019;7:100419. https://doi.org/10.1016/j.mtla.2019.100419.

[37] Kubaschewski O, Alcock C, Spencer P. Materials Thermochemistry. Pergamon Press, New York, 1993.

[38] Nishiyama N, Inoue A. Glass transition behavior and viscous flow working of $Pd_{40}Cu_{30}Ni_{10}P_{20}$ amorphous alloy. Mater Trans JIM 1999;40:64-71. https://doi.org/10.2320/matertrans1989.40.64.

[39] Turnbull D, Cohen MH. Concerning reconstructive transformation and formation of glass. J Chem Phys 1958;29:1049-1054. https://doi.org/10.1063/1.1744654.

[40] Lu ZP, Liu CT. A new glass-forming ability criterion for bulk metallic glasses. Acta Mater 2002;50: 3501-3512. https://doi.org/10.1016/s1359-6454(02)00166-0.

[41] Luo Q, Wang WH. Magnetocaloric effect in rare earth-based bulk metallic glasses. J Alloys Compd 2010;495:209-216. https://doi.org/10.1016/j.jallcom.2010.01.125.

[42] Gschneidner KA Jr, Pecharsky VK. Magnetocaloric materials. Annu Rev Mater Sci 2000;30:387-429. https://doi.org/10.1146/annurev.matsci.30.1.387.

[43] Na JH, Demetriou MD, Floyd M, Hoff A, Garrett GR, Johnson WL. Compositional landscape for glass formation in metal alloys. Proc Natl Acad Sci USA 2014;111:9031-9036. https://doi.org/10.1073/pnas.1407780111.

[44] Angell CA. Formation of glasses from liquids and biopolymers. Science 1995;267:1924-1935.

https://doi.org/10.1126/science.267.5206.1924.

[45] Jiang MQ, Naderi M, Wang YJ, Peterlechner M, Liu XF, Zeng F, Jiang F, Dai LH, Wilde G. Thermal expansion accompanying the glass-liquid transition and crystallization. Aip Adv 2015;5:127133. https://doi.org/10.1063/1.4939216.

[46] Du Y, Zhou Q, Jia Q, Shi YD, Wang HF, Wang J. Imparities of shear avalanches dynamic evolution in a metallic glass. Mater Res Lett 2020;8:357-363. https://doi.org/10.1080/21663831.2020.1771450.

[47] Zhao YL, Yang T, Han B, Luan JH, Chen D, Kai W, Liu CT, Kai JJ. Exceptional nanostructure stability and its origins in the CoCrNi-based precipitation-strengthened medium-entropy alloy. Mater Res Lett 2019;7:152-158. https://doi.org/10.1080/21663831.2019.1568315.

[48] Fujita T, Konno K, Zhang W, Kumar V, Matsuura M, Inoue A, Sakurai T, Chen MW. Atomic-scale heterogeneity of a multicomponent bulk metallic glass with excellent glass forming ability. Phys Rev Lett 2009;103:075502. https://doi.org/10.1103/PhysRevLett.103.075502.

[49] Guan PF, Fujita T, Hirata A, Liu YH, Chen MW. Structural origins of the excellent glass forming ability of $Pd_{40}Ni_{40}P_{20}$. Phys Rev Lett 2012;108:175501. https://doi.org/10.1103/PhysRevLett.108.175501.

[50] Fan GY, Cowley JM. Autocorrelation analysis of high-resolution electron -micrographs of near-amorphous thin-films. Ultramicroscopy 1985;17:345-355. https://doi.org/10.1016/0304-3991(85)90201-3.

[51] Liu XJ, Chen GL, Hou HY, Hui X, Yao KF, Lu ZP, Liu CT. Atomistic mechanism for nanocrystallization of metallic glasses. Acta Mater 2008;56:2760-2769. https://doi.org/10.1016/j.actamat.2008.02.019.

[52] Sarac B, Ivanov YP, Chuvilin A, Schoeberl T, Stoica M, Zhang Z, Eckert J. Origin of large plasticity and multiscale effects in iron-based metallic glasses. Nat Commun 2018;9:1333. https://doi.org/10.1038/s41467-018-03744-5.

[53] Wang QQ, Zhou J, Zeng QS, Zhang GL, Yin KB, Liang T, Yang WM, Stoica M, Sun LT, Shen BL. Ductile Co-based bulk metallic glass with superhigh strength and excellent soft magnetic properties induced by modulation of structural heterogeneity. Materialia 2020;9:100561. https://doi.org/10.1016/j.mtla.2019.100561.

[54] Wang Q, Liu CT, Yang Y, Dong YD, Lu J. Atomic-Scale Structural Evolution and Stability of Supercooled Liquid of a Zr-Based Bulk Metallic Glass. Phys Rev Lett 2011;106:215505. https://doi.org/10.1103/PhysRevLett.106.215505.

[55] Ma E, Ding J. Tailoring structural inhomogeneities in metallic glasses to enable tensile ductility at room temperature. Mater Today 2016;19:568-579. https://doi.org/10.1016/j.mattod.2016.04.001.

[56] Yuan CC, Lv ZW, Pang CM, Wu XL, Lan S, Lu CY, Wang LG, Yu HB, Luan JH, Zhu WW, Zhang GL, Liu Q, Wang XL, Shen BL. Atomic-scale heterogeneity in large-plasticity Cu-doped metallic glasses. J Alloys Compd. 2019;798:517-522. https://doi.org/10.1016/j.jallcom.2019.05.282.

[57] Sheng HW, Cheng YQ, Lee PL, Shastri SD, Ma E. Atomic packing in multicomponent aluminum-based metallic glasses. Acta Mater 2008;56:6264-6272. https://doi.org/10.1016/j.actamat.2008.08.049.

[58] Miracle DB. A structural model for metallic glasses. Nat Mater 2004;3:697-702. https://doi.org/10.1038/nmat1219.

[59] Sheng HW, Luo WK, Alamgir FM, Bai JM, Ma E. Atomic packing and short-to-medium-range order in metallic glasses. Nature 2006;439:419-425. https://doi.org/10.1038/nature04421.

[60] Lee HJ, Cagin T, Johnson WL, Goddard WA. Criteria for formation of metallic glasses: The role of atomic size ratio. J Chem Phys 2003;119:9858-9870. https://doi.org/10.1063/1.1615494.

[61] Egami T, Waseda Y. Atomic size effect on the formability of metallic glasses. J. Non-Cryst Solids 1984;64:113-134. https://doi.org/10.1016/0022-3093(84)90210-2.

[62] Miracle DB, Sanders WS, Senkov ON. The influence of efficient atomic packing on the constitution of metallic glasses. Philos Mag 2003;83:2409-2428. https://doi.org/10.1080/1478643031000098828.

[63] Saida J, Matsushita M, Inoue A. Direct observation of icosahedral cluster in $Zr_{70}Pd_{30}$ binary glassy alloy. Appl Phys Lett 2001;79:412-414. https://doi.org/10.1063/1.1385802.

[64] Soklaski R, Nussinov Z, Markow Z, Kelton KF, Yang L. Connectivity of icosahedral network and a dramatically growing static length scale in Cu-Zr binary metallic glasses. Phy Rev B 2013;87:184203. https://doi.org/10.1103/PhysRevB.87.184203.

[65] Li MZ, Wang CZ, Hao SG, Kramer MJ, Ho KM. Structural heterogeneity and medium-range order in Zr_xCu_{100-x} metallic glasses. Phys Rev B 2009;80:184201. https://doi.org/10.1103/PhysRevB.80.184201.

[66] Cheng YQ, Ding J, Ma E. Local Topology vs. Atomic-Level Stresses as a Measure of Disorder: Correlating Structural Indicators for Metallic Glasses. Mater Res Lett 2013;1:3-12 https://doi.org/12. 10.1080/21663831.2012.722759.

[67] Yang ZJ, Tang L, Wen TQ, Ho KM, Wang CZ. Effects of Si solute on the glass formation and atomic structure of Pd liquid. J Phys-Condens Mat 2019;31:135701. https://doi.org/10.1088/1361-648X/aafd02.

Table 1

The onset temperature of glass transition (T_g), of crystallization (T_x) and liquidus temperature (T_l) under the heating rate of 40 K/min as well as the parameters including the width of supercooled liquid region (ΔT_x), reduced glass transition temperature (T_{rg}) and gamma parameter (γ) for the $(Gd_{0.2}Dy_{0.2}Er_{0.2}Co_{0.2}Al_{0.2})_{100-x}Si_x$ (x = 0, 1, 2, 3 and 4) BMG samples with the diameter of 1 mm.

Si content (at.%)	d_c (mm)	T_g (K)	T_x (K)	ΔT_x (K)	T_l (K)	T_{rg}	γ
0	1.5	610	652	42	1053	0.579	0.392
0.5	8.5	618	682	64	1049	0.589	0.409
1	6	624	694	70	1061	0.588	0.412
2	5	629	697	68	1133	0.555	0.396
3	3	636	694	58	1147	0.554	0.389
4	1	640	695	55	1186	0.540	0.381

Table 2

Magnetocaloric parameters inclusive of Curie temperature (T_C), maximum value of magnetic entropy change ($|\Delta S_M^{pk}|$) under magnetic fields of 2 and 5 T, as well as relative cooling power (*RCP*) under a magnetic field of 5 T, and fitting parameters for the C_p data obtained from Eqs. (1) and (2) for the HESix (x = 0, 0.5, 1 and 3) BMG samples.

Composition	T_C (K)	$\left\|\Delta S_M^{pk}\right\|$ (J kg^{-1}K^{-1})		*RCP* (J kg-1)	*a*	*b*	*c*	*d*
		2 T	5 T					
HESi0	44	4.1	9.1	619	0.00751	6.366×10^{6}	-0.00666	1.416×10^{-5}
HESi0.5	44	4.6	9.4	620	0.00644	7.211×10^{6}	-0.00912	2.429×10^{-5}
HESi1	44	4.1	9.2	616	0.00855	8.018×10^{6}	-0.01106	2.141×10^{-5}
HESi3	44	4.0	9.0	585	0.00948	9.087×10^{6}	-0.00966	2.051×10^{-5}

Figure Captions

Fig. 1 (a) and (b) DSC traces of $(Gd_{0.2}Dy_{0.2}Er_{0.2}Co_{0.2}Al_{0.2})_{100-x}Si_x$ BMG samples with a diameter of 1 mm. (c) XRD patterns of the as-cast HESi0.5 samples with diameters of 5 and 8.5 as well as HESi1 samples with diameters of 3 and 6 mm. (d) XRD patterns of the as-cast HESi0, HESi0.5 and HESi3 samples with the diameter larger than the critical diameter of corresponding BMGs.

Fig. 2 Isothermal crystallization curves for HESix BMG samples. The incubation time (t_{in}) is marked with arrows.

Fig. 3 Overview of specific heat capacities versus temperature for (a) HESi0, (b) HESi0.5, (c) HESi1 and (d) HESi3 samples. The data points for the crystal are denoted with filled circles, the glassy state with half-filled diamonds and the liquid state with unfilled triangles. The data of liquid (dashed line) and crystal (solid line) are fitted with Eqs. (1) and (2), respectively.

Fig. 4 Temperature dependence of free energy difference between liquid and crystal (ΔG^{l-x}) for HESix alloys. The temperature axis is normalized with their respective melting temperatures T_{m}.

Fig. 5 (a) TMA traces of HESix BMG samples with a diameter of 1.5 mm and a height of 3 mm. (b) Angell plots of the VFT fits with the typical abscissa of the inverse temperature that is nominated by T_g^* (the temperature at which the viscosity has a value of 10^{12} Pa s) for HESix samples. The fitting parameters D^* and T_0 are listed in the inserted table.

Fig. 6 SEM image and corresponding EDS mappings of (a) HESi0, (b) HESi0.5 and (c) HESi3 BMG samples, the size of each mapping is 20 × 20 μm^2. HAADF STEM image and corresponding EDS mappings for (d) HESi0, (e) HESi0.5 and (f) HESi3 BMG samples, the size of distribution mapping is 100 × 100 nm^2.

Fig. 7 The corresponding distribution signals of different elements along the diagonal of EDS mappings in Fig. 6(d)-(f) for (a) HESi0, (b) HESi0.5 and (c) HESi3 BMG samples, respectively.

Fig. 8 3D-APT reconstruction of all elements in the tip taken from (a) HESi0, (b) HESi0.5 and (c) HESi3 BMG samples. (e) and (f) One-dimensional concentration profiles taken along the length direction of the tip such as (d) for HESi0 sample. (g) and (h) Frequency distribution analysis obtained from the observed experimental results and binomial simulation. The quality of the fit is quantified using typical parameters as listed in the inserted tables, where n_d is the number of degrees of freedom for a given ion and μ is the normalized homogenization parameter. All the scale bars correspond to 25 nm.

Fig. 9 HRTEM images with the corresponding SAED patterns in the insets for (a) HESi0, (b) HESi0.5 and (c) HESi3 BMG samples. (d)-(f) are the auto-correlation processed images corresponding to the selected areas in (a)-(c) respectively. The size of each segment is 1.811 × 1.811 nm^2.

Fig. 10 (a) RDFs of HESi0, HESi0.5 and HESi3 BMG samples obtained from the corresponding SAED patterns in the insets of Fig. 9. (b) Magnified first peak of RDFs.

Fig. 11 (a)-(c) are the IFT-filtered images of the selected areas (yellow squares) in Fig. 9(a)-(c), respectively, showing the atomic configurations for an amorphous region with ordered clusters. The insets are the corresponding FT diffraction patterns.

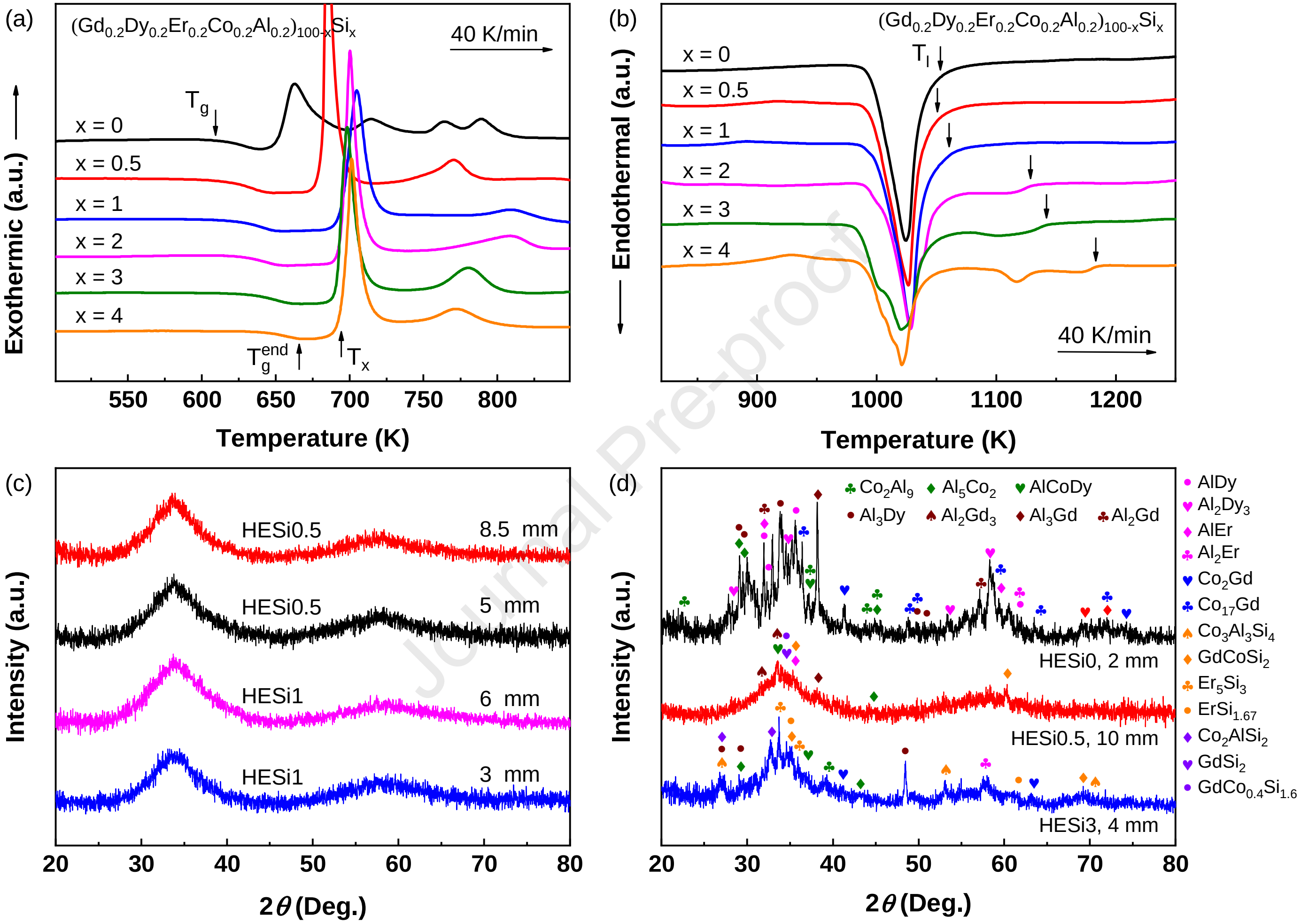
(a)
$(Gd_{0.2}Dy_{0.2}Er_{0.2}Co_{0.2}Al_{0.2})_{100-x}Si_x$
40 K/min
T_g
x = 0
x = 0.5
x = 1
x = 2
x = 3
x = 4
T_g^{end}
T_x
Exothermic (a.u.)
550
600
650
700
750
800
Temperature (K)
(b)
$(Gd_{0.2}Dy_{0.2}Er_{0.2}Co_{0.2}Al_{0.2})_{100-x}Si_x$
T_l
x = 0
x = 0.5
x = 1
x = 2
x = 3
x = 4
40 K/min
Endothermal (a.u.)
900
1000
1100
1200
Temperature (K)
(c)
HESi0.5 8.5 mm
HESi0.5 5 mm
HESi1 6 mm
HESi1 3 mm
Intensity (a.u.)
20
30
40
50
60
70
80
2θ (Deg.)
(d)
Co_2Al_9
Al_5Co_2
AlCoDy
Al_3Dy
Al_2Gd_3
Al_3Gd
Al_2Gd
AlDy
Al_2Dy_3
AlEr
Al_2Er
Co_2Gd
$Co_{17}Gd$
$Co_3Al_3Si_4$
$GdCoSi_2$
Er_5Si_3
$ErSi_{1.67}$
Co_2AlSi_2
$GdSi_2$
$GdCo_{0.4}Si_{1.6}$
HESi0, 2 mm
HESi0.5, 10 mm
HESi3, 4 mm
Intensity (a.u.)
20
30
40
50
60
70
80
2θ (Deg.)

Fig. 1

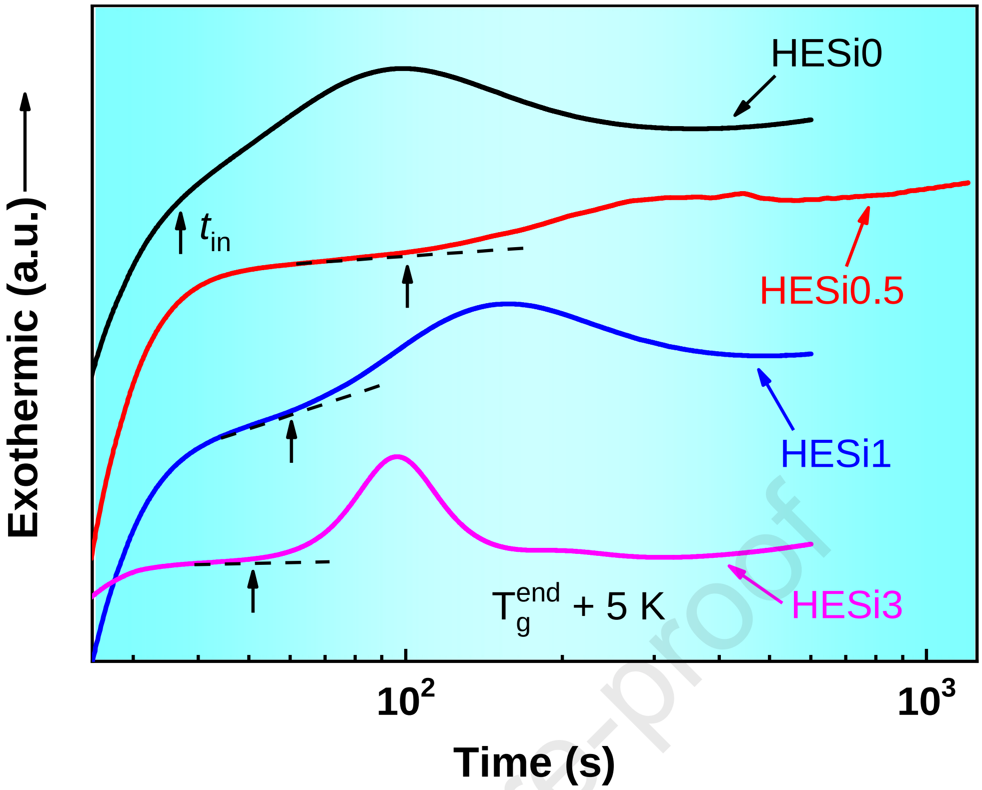
Exothermic (a.u.)
Time (s)
10^2
10^3
HESi0
HESi0.5
HESi1
HESi3
t_in
T_g^end + 5 K

Fig. 2

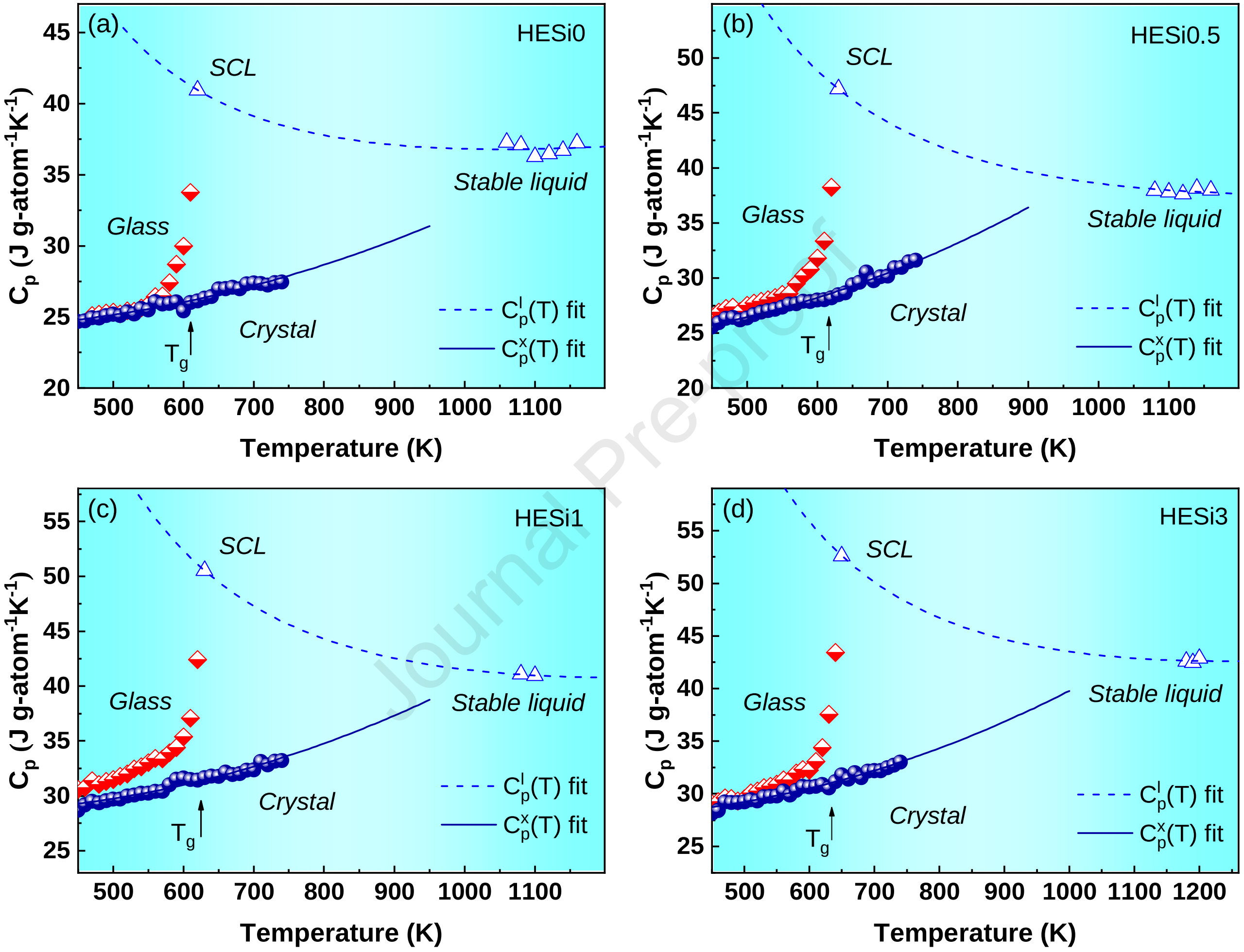
(a)
HESi0
SCL
Stable liquid
Glass
Crystal
T_g
$C_p^l(T)$ fit
$C_p^x(T)$ fit
(b)
HESi0.5
(c)
HESi1
(d)
HESi3
C_p (J g-atom^{-1}K^{-1})
Temperature (K)
500
600
700
800
900
1000
1100
1200
20
25
30
35
40
45
50
55

Fig. 3

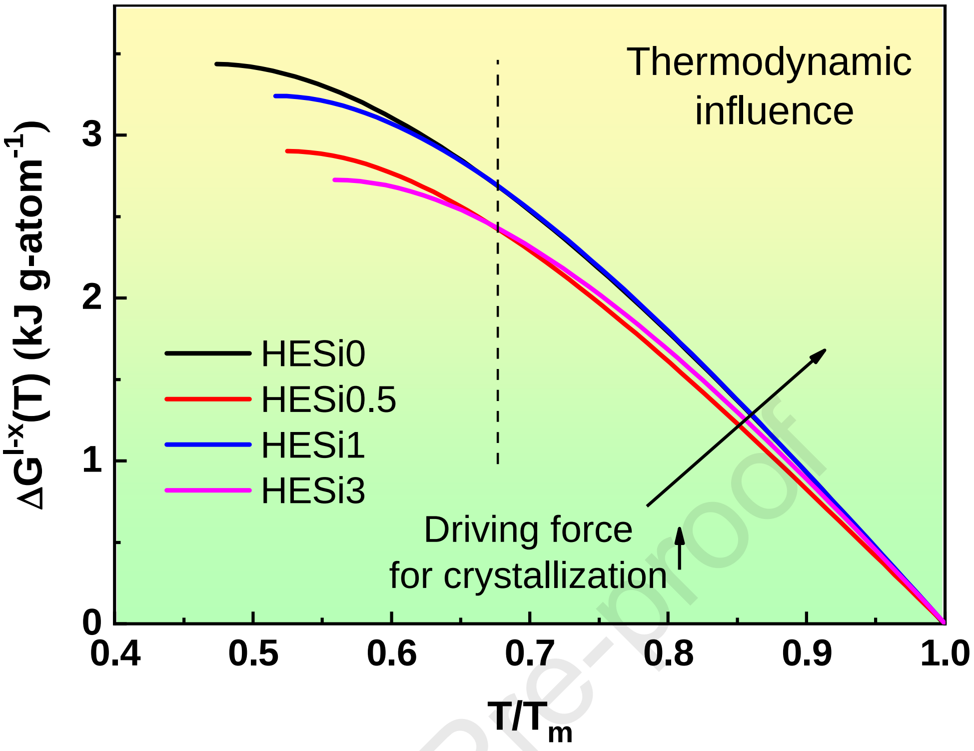
Thermodynamic
influence
HESi0
HESi0.5
HESi1
HESi3
Driving force
for crystallization
$\Delta G^{l\text{-}x}(T)$ (kJ g-atom^{-1})
0
1
2
3
0.4
0.5
0.6
0.7
0.8
0.9
1.0
T/T_m

Fig. 4

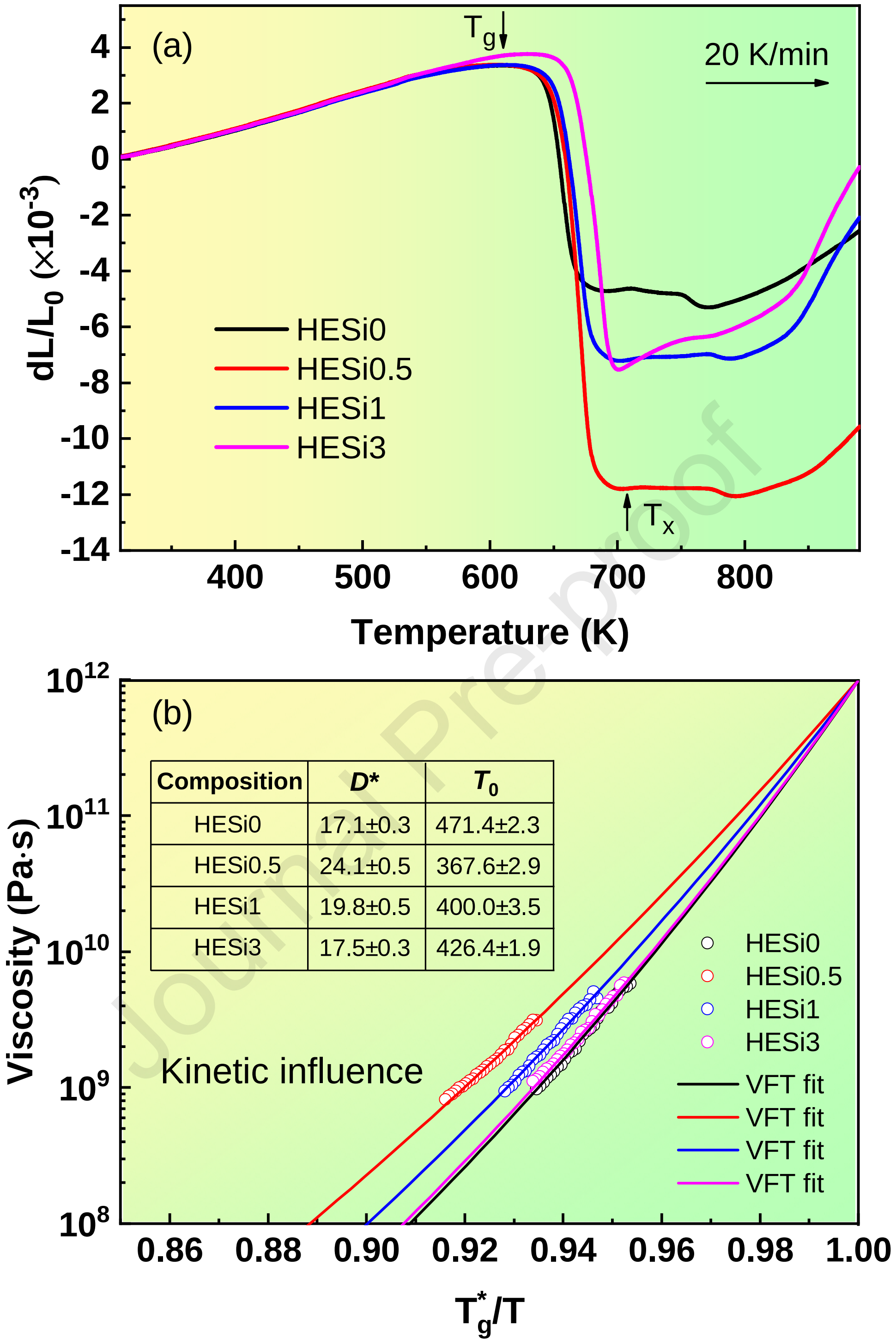

Composition	***D****	***T*₀**
HESi0	17.1±0.3	471.4±2.3
HESi0.5	24.1±0.5	367.6±2.9
HESi1	19.8±0.5	400.0±3.5
HESi3	17.5±0.3	426.4±1.9

Fig. 5

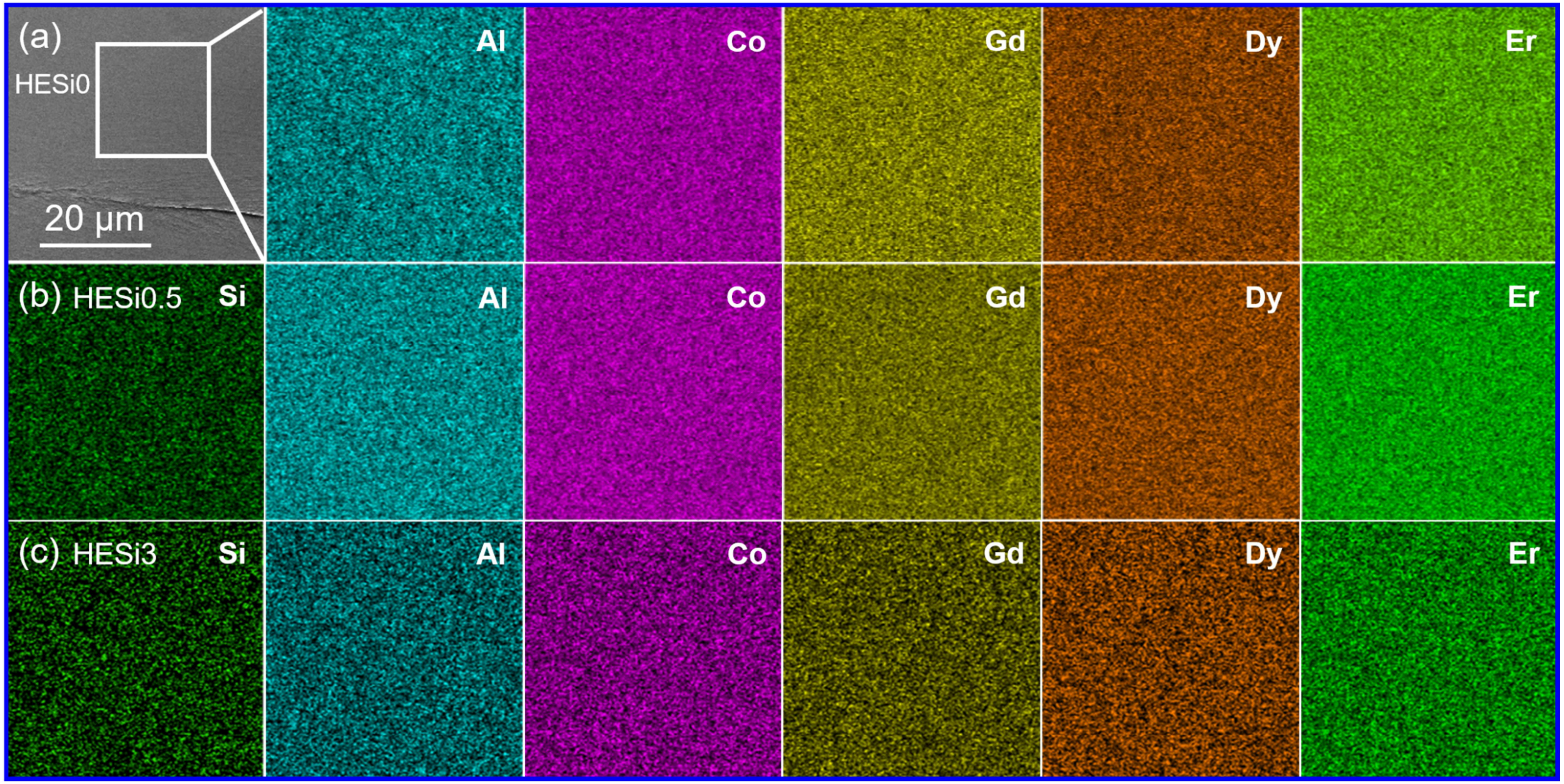
(a)
HESi0
20 μm
Al
Co
Gd
Dy
Er
(b) HESi0.5
Si
Al
Co
Gd
Dy
Er
(c) HESi3
Si
Al
Co
Gd
Dy
Er

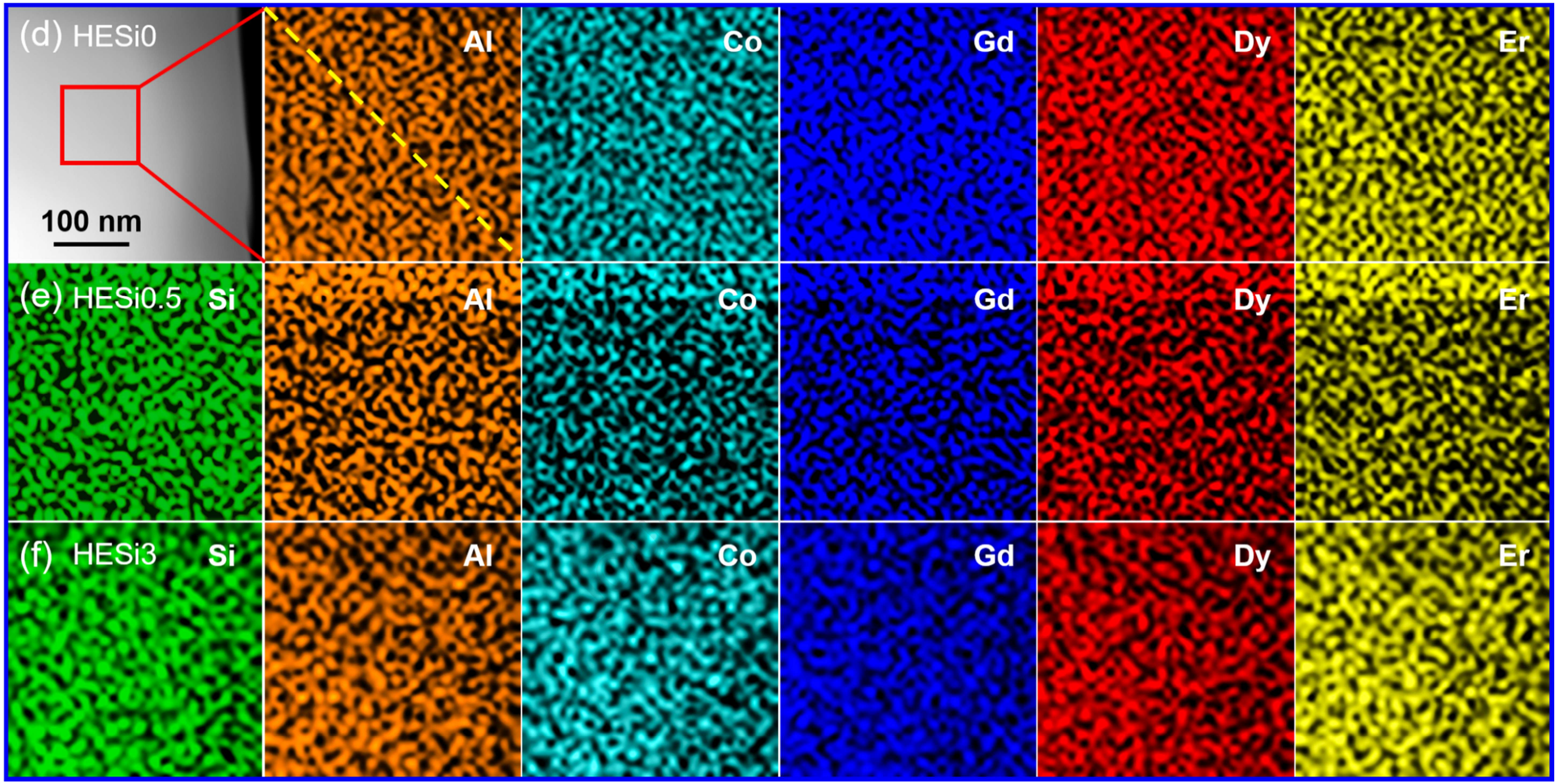
(d) HESi0
100 nm
Al
Co
Gd
Dy
Er
(e) HESi0.5
Si
Al
Co
Gd
Dy
Er
(f) HESi3
Si
Al
Co
Gd
Dy
Er

Fig. 6

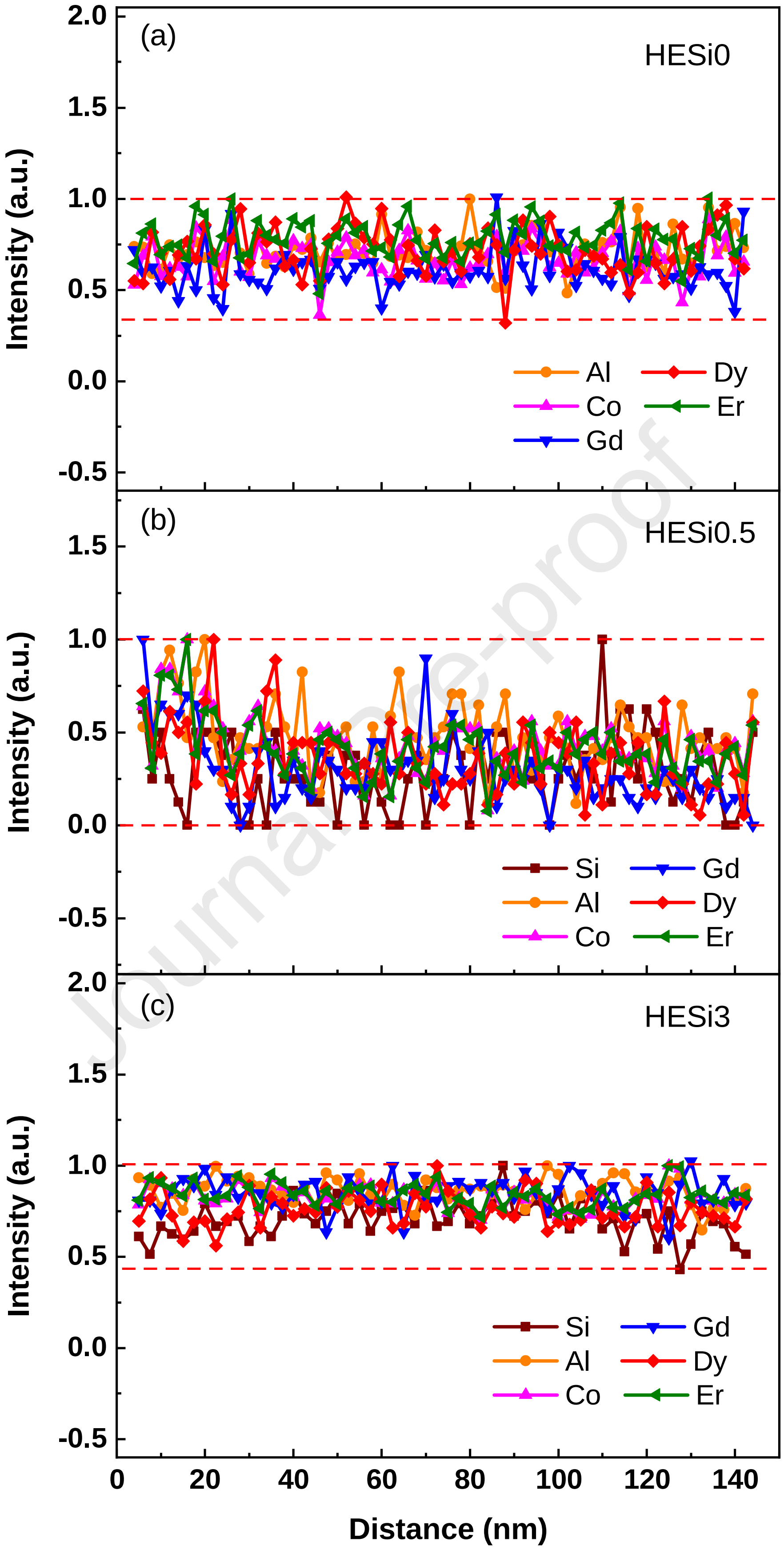
(a)
HESi0
Al
Dy
Co
Er
Gd
(b)
HESi0.5
Si
Gd
Al
Dy
Co
Er
(c)
HESi3
Si
Gd
Al
Dy
Co
Er
Intensity (a.u.)
2.0
1.5
1.0
0.5
0.0
-0.5
0
20
40
60
80
100
120
140
Distance (nm)

Fig. 7

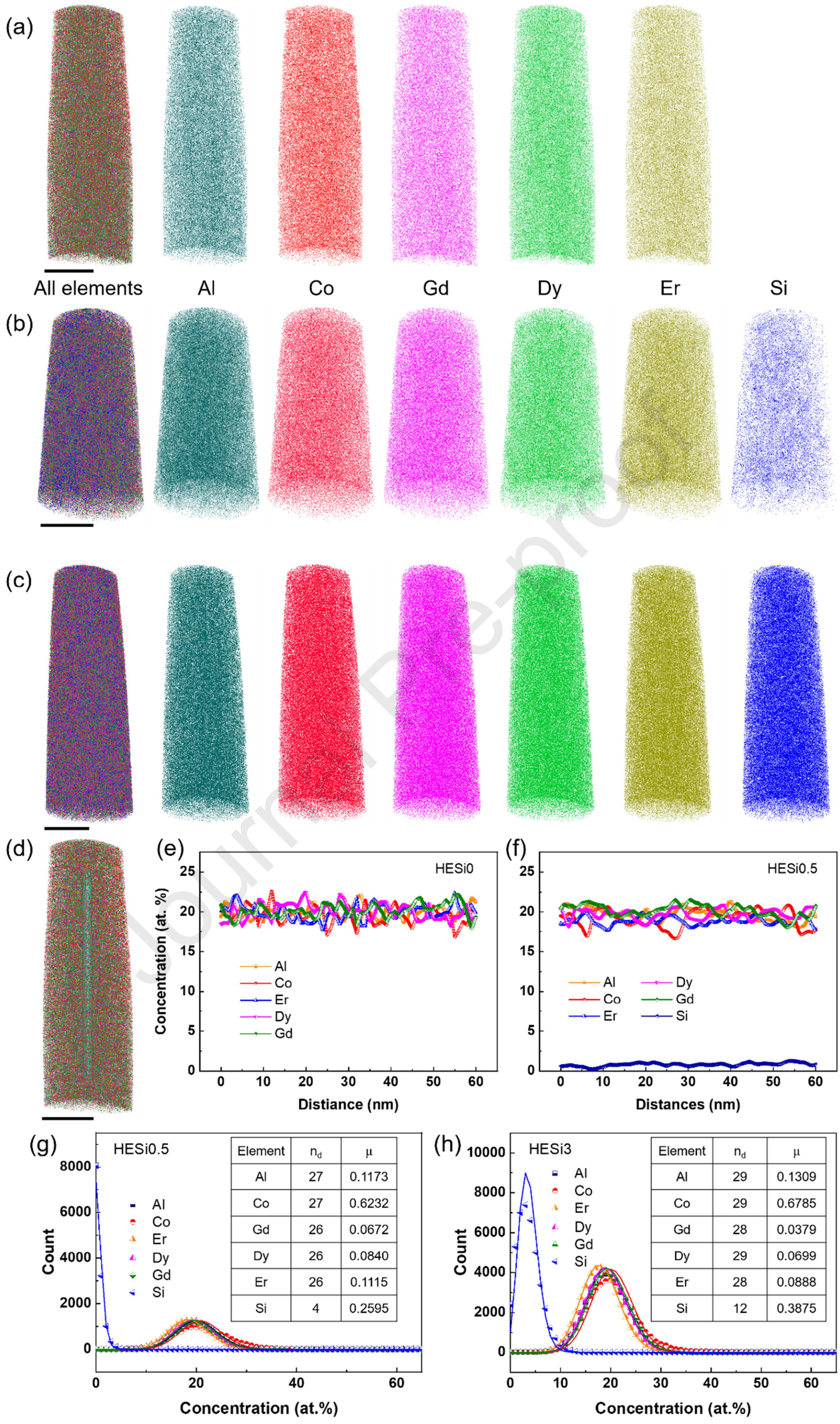

Element	n_d	μ
Al	27	0.1173
Co	27	0.6232
Gd	26	0.0672
Dy	26	0.0840
Er	26	0.1115
Si	4	0.2595

Element	n_d	μ
Al	29	0.1309
Co	29	0.6785
Gd	28	0.0379
Dy	29	0.0699
Er	28	0.0888
Si	12	0.3875

Fig. 8

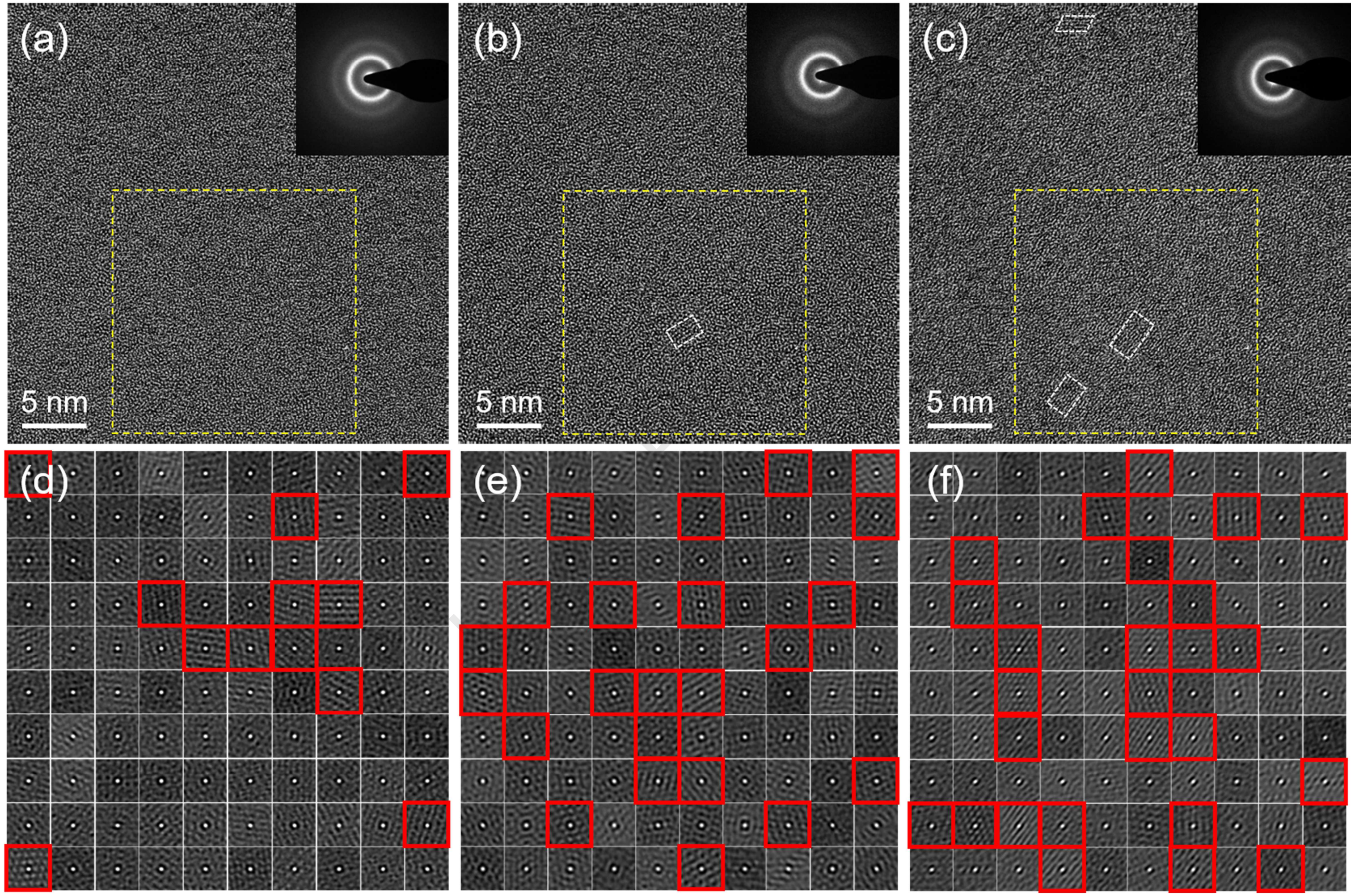

Fig. 9

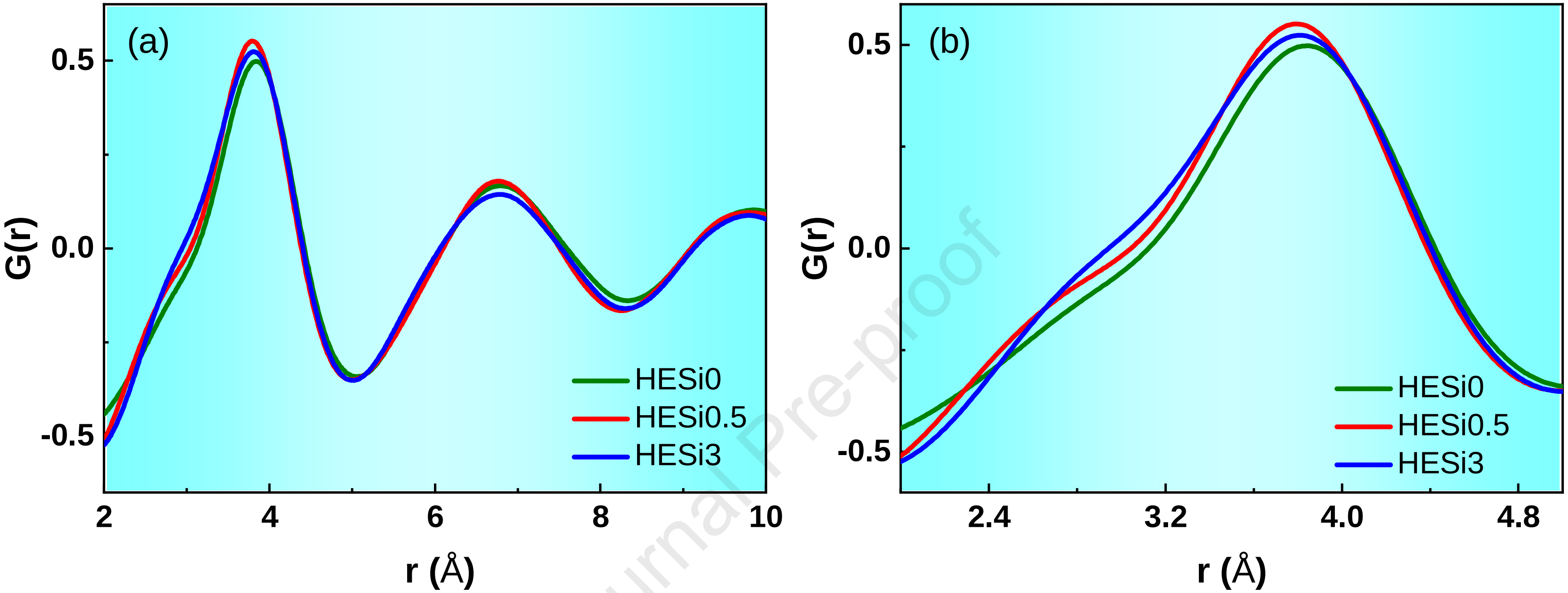

Fig. 10

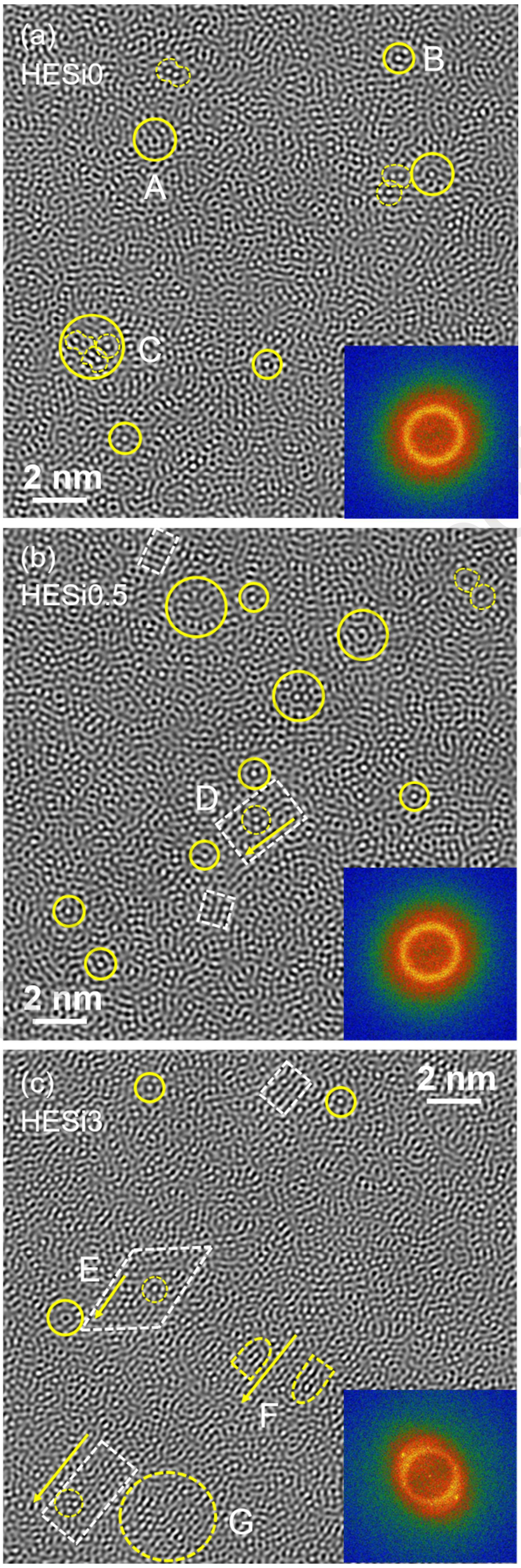

Fig. 11

Declaration of interests

☒ The authors declare that they have no known competing financial interests or personal relationships that could have appeared to influence the work reported in this paper.

☐The authors declare the following financial interests/personal relationships which may be considered as potential competing interests: